Title

Characterization of Porous Materials by Fluorescence Correlation Spectroscopy Super-resolution Optical Fluctuation Imaging

Journal

ACS Nano, 9(9)

ISSN

1936-0851

Authors

Kisley, Lydia
Brunetti, Rachel
Tauzin, Lawrence J
et al.

Publication Date

2015-09-22

DOI

10.1021/acsnano.5b03430

Characterization of Porous Materials by fcsSOFI

Lydia Kisley,[1] Rachel Brunetti,[2] Lawrence J. Tauzin,[1] Bo Shuang,[1] Xiyu Yi,[3] Alec W. Kirkeminde,[4] Daniel A. Higgins,[4] Shimon Weiss,[3,5,6] Christy F. Landes,[1,7]**

[1] Department of Chemistry, Rice University, Houston, TX 77251

[2] Department of Physics, Scripps College, Claremont, CA 91711

[3] Department of Chemistry and Biochemistry, University of California Los Angeles, Los Angeles, CA 90095

[4] Department of Chemistry, Kansas State University, 213 CBC Building, Manhattan, Kansas 66506-0401, United States

[5] Department of Physiology, University of California Los Angeles, Los Angeles, CA 90095

[6] California NanoSystems Institute, University of California Los Angeles, Los Angeles, CA 90095

[7] Department of Electrical and Computer Engineering, Rice University, Houston, TX 77251

KEYWORDS: correlation, super-resolution, fluorescence microscopy, diffusion, liquid crystal, hydrogel

ABSTRACT

Porous materials such as cellular cytosol, hydrogels, and block copolymers have nanoscale features that determine macroscale properties. Characterizing the structure of nanopores is difficult with current techniques due to imaging, sample preparation, and computational challenges. We introduce a super-resolution optical imaging technique that simultaneously characterizes the nanometer dimensions of and diffusion dynamics within porous structures by correlating stochastic fluctuations from diffusing fluorescent probes in the pores of the sample, dubbed here as “fcsSOFI.” Simulations demonstrate that structural features and diffusion properties can be accurately obtained at sub-diffraction-limited resolution. We apply our technique to image agarose hydrogels and aqueous lyotropic liquid crystal gels. The heterogeneous pore resolution is improved by up to a factor of two and diffusion coefficients are accurately obtained through our method compared to diffraction-limited fluorescence imaging and single particle tracking. Moreover, fcsSOFI allows for rapid and high-throughput characterization of porous materials. fcsSOFI could be applied to soft porous environments such hydrogels, polymers, and membranes, in addition to hard materials such as zeolites and mesoporous silica.

A wide range of both natural and synthetic materials derive their function from nanoscale porous structure.[1-11] Despite the importance of these materials, a detailed understanding of the relationship between nanoscale structure and the functional capabilities is lacking due to insufficient characterization techniques. Electron and force microscopy methods have experimental requirements that distort and even destroy the porous structure.[12] Ensemble techniques report average pore properties, losing information about the spatial heterogeneity.[13] Microrheology provides local viscoelastic information, but lacks visual spatial resolution and requires a high computational cost to track and analyze many particles.[14] An optimized analytical method would provide *in situ* characterization of the relationship between heterogeneous nanoscale structure and functional properties such as transport or adsorption.

Correlation analysis provides important spatial and diffusion details about materials. Super-resolution Optical Fluctuation Imaging (SOFI)[15] uses correlation analysis to achieve spatial resolution below the diffraction limit.[16-19] SOFI correlates optical fluctuations from individual switching emitters, and pixels with isolated emitters will have a highly correlated signal compared to areas with mixed signal from multiple emitters. SOFI offers advantages over other localization-based super-resolution techniques because it has a broader tolerance for emitter density, signal-to-background ratio (SBR), point spread function (PSF) shape, and user-input requirements.[20, 21] Correlation analysis can also resolve and quantify diffusion dynamics with fluorescence

correlation spectroscopy (FCS)[22] and imaging analogues.[23-26] Emitters diffuse through a focal volume, creating spontaneous fluctuations recorded in a temporal photon series. The decay of the temporal autocorrelation function of the photon trace is analyzed to extract information on the type and rate of diffusion.

Here we combine SOFI with FCS to yield a powerful new method, named fcsSOFI, which can simultaneously provide super-resolution optical imaging together with diffusion dynamics of probe molecules in porous structures. We correlate fluctuations from diffusing probes within the negative, porous space of the sample. A super-resolution image of the pore sizes is obtained from the amplitude of the correlation curve. Diffusion properties are mapped at the diffraction limit by fitting the correlation curve. Image fusion produces a final map of the nanoscale spatial and diffusion information. The theoretical framework for stochastic diffusion to produce super-resolved images is provided and the technique is demonstrated by simulation. We apply our analysis to quantify the heterogeneous pore distribution and diffusion of fluorescent probes within agarose hydrogels and lyotropic liquid crystals. Our results are compared to diffraction-limited imaging and localization-based single particle tracking (SPT) and demonstrate that fcsSOFI provides an objective, sensitive, high-throughput analysis, especially under challenging experimental conditions with low signal or high density of emitters.

RESULTS AND DISCUSSION

fcsSOFI theory and analysis

The theory of obtaining sub-diffraction-limited resolution by correlation analysis relies on imaging multiple radiant emitters diffusing within a porous material, thus creating fluctuations in the signal based on their stochastic and independent diffusion. The signal, F, detected at a given pixel position, r, and frame time, t, from emitters nearby is:

$$(1) F(r,t) = \int dr_1 U(r - r_1) \varepsilon_1 B_1(t)$$

where $U(r - r_1)$ is the PSF centered at r_1, ε_1 is the constant brightness of the emitter, and $B_1(t)$ is the probability of an emitter being located at r_1 at t. In this work, emitters are fluorescent beads whose brightness is approximately constant during measurements, but any material that produces an optical signal could be used as a probe as long as the signal fluctuates with time due to diffusion (see Supporting Information). The fluctuation of the signal over time, $\delta F(r,t)$, is caused by $B(t)$:

$$(2) \delta F(r,t) = \int dr_1 U(r - r_1) \varepsilon_1 \left[B_1(t) - ¿ B_1(t) ¿_t \right] = \int dr_1 U(r - r_1) \varepsilon_1 \delta B_1(t)$$

where $¿ \bullet ¿_t$ represents the average over time. The autocorrelation at a given pixel k is calculated by:

$$(3) G_2(k,\tau) = \int_{r \in pixel_k} dr \bullet G_2(r,\tau) = \int_{r \in pixel_k} dr \bullet <\delta F(r, t+\tau) \bullet \delta F(r,t) ¿_t$$

$$¿ \int_{r \in pixel_k} dr \int dr_1 U(r - r_1) \int dr_2 U(r - r_2) \varepsilon_1 \varepsilon_2 <\delta B_2(t+\tau) \delta B_1(t)> ¿ = \int_{r \in pixel_k} dr \int dr_1 U(r - r_1) \int d(r_2 - r_1) U ¿$$

$$(4) G_2(k,\tau) \int_{r\in pixel_k} dr \int dr_1 U(r-r_1) \times \left[U(r-r_1) \otimes \exp\left(\frac{-(r-r_1)^2}{4D\tau} \right) \right] \varepsilon_1 \varepsilon_2$$

where ¿C>¿ is the average concentration of diffusing emitters, ⊗ stands for convolution, and τ is the time lag. We use a Gaussian function to approximate the PSF:

$$(5) U(r) = \exp\left(\frac{-x^2+y^2}{2\sigma_{xy}^2} - \frac{z^2}{2\sigma_z^2} \right)$$

The analysis below considers resolution enhancement in 2D only (x and y components), as our experimental data can be considered a projection of the ~85 nm z-dimension focal depth onto 2D.[27] After the 2nd order autocorrelation the equivalent 2D width of the PSF will be:

$$(6) \frac{1}{\sigma_{new}^2} = \frac{1}{\sigma_{xy}^2} + \frac{1}{\sigma_{xy}^2 + 2D\tau}$$

so that $\frac{\sigma_{xy}}{\sqrt{2}} < \sigma_{new} < \sigma_{xy}$. This proves that the resolution is indeed improved using 2nd order autocorrelation fcsSOFI. Further improvement in spatial resolution at the boundaries of adjacent pores is described in the Supporting Information. Specifically, for materials with 1D structure, diffusion is limited to the longitudinal direction only, such that the transverse resolution improvement will achieve the same resolution improvement as SOFI. At the limits of diffusion when $D=\infty$, there is no resolution improvement; and when $D=0$, the resolution improvement is maximized to be the same as 2nd order autocorrelation SOFI obtained for static emitters. However, both cases are experimentally impractical as a large D results in low signal and $D=0$ causes

zero intensity fluctuations at each pixel for the constant, non-blinking emitters, making fcsSOFI measurement and analysis impossible. Therefore, fcsSOFI resolution capabilities lie between the diffraction limit and SOFI. Like FCS measurements, the concentration of emitters and the average diffusion coefficient need to be carefully selected to optimize the performance (Figure S1).

As a demonstration in this work, we perform 2nd order autocorrelation of the intensity transient at each pixel, which results in an image with a resolution improvement close to $\sim < \sqrt{2}$ by employing the value of $G_2(k, \tau)$ at the first time lag, $\tau = dt = 1$ frame, where dt is the time lag between frames (Figure S2).[15] A blind deconvolution[28] is then performed to achieve a final resolution enhancement of $\sim < 2$ (Figure S2). It is important to note that higher order autocorrelation and cross-correlation would improve the resolution even further,[15, 20] to a range of $\frac{\sigma_{xy}}{\sqrt{n}} < \sigma_n < \sigma_{xy}$ where n is the order of the correlation, but require overcoming computational challenges (computation time and memory usage scale as the correlation order squared)[15] and have brightness/sampling artifacts that cause the pixel intensities to vary over a very large dynamic range (spatially highlighting bright areas and masking dim ones).[2, 15] For proof-of-concept, we demonstrate here only 2nd order autocorrelation and deconvolution analysis, similar to use of 2nd order autocorrelation SOFI reported in the literature.[2]

Super-resolution distributions of the diffusion dynamics are obtained from curve fitting analysis and image fusion. Using fitting models for Brownian diffusion reported in previous imaging extensions of FCS,[24, 25] the resulting diffusion coefficient at each pixel is spatially mapped (see Methods). As with most microscopy techniques, when imaging 3D samples as a 2D projection, the apparent diffusion coefficient can be underestimated due to movement along the z-axis. However, because SOFI is less sensitive to out-of-plane motions compared to wide-field imaging,[29] the impact of 3D-to-2D projection is correspondingly reduced. Additionally, the reduced focal depth of SOFI is advantageous for quantifying 3D motion when combined with, for example multi-focal imaging.[30] A super-resolution map of diffusion information is formed by fusing[31] the spatial and diffusion results on a hue-saturation-value (HSV) colormap. The hue is the normalized log of the diffusion coefficient. The saturation is the normalized super-resolution spatial information. The HSV matrix is then converted to red-green-blue (RGB) matrix to produce the final super-resolution map of diffusion characteristics.

Demonstration of fcsSOFI by simulation

Simulations were used to demonstrate super-resolution imaging of two neighboring pores (Figure 1). Brownian diffusion was simulated with different diffusion coefficients in each pore, D_{left} = 1 x 10^5 nm^2/s and D_{right} = 1 x 10^4 nm^2/s (Movie S1). A relatively low SBR was used to

simulate data that occurs when imaging single molecules in cellular environments where high levels of autofluorescence are present and low quantum yield emitters are required for biocompatibility.[32] Sample diffraction-limited images are shown in Figure 1a. Resulting intensity

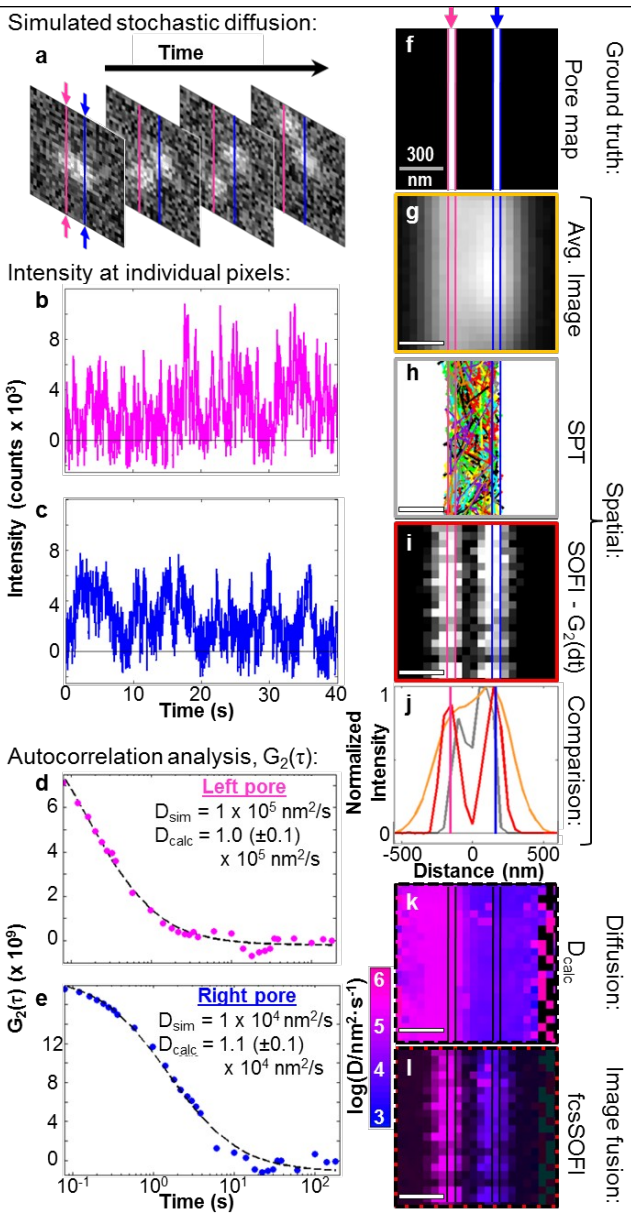

Figure 1. fcsSOFI analysis of simulated diffraction-limited diffusion improves spatial resolution with accurate diffusion properties. (**a-e**) Steps of fcsSOFI. (**a**) Example frames of two emitters undergoing simulated 1D Brownian diffusion in neighboring pores that are unresolvable by the diffraction limit. Pore locations are indicated by pink and blue

arrows/colored lines. (**b, c**) Example intensity transients from one pixel in the (**b**) left and (**c**) right pores. (**d, e**) Autocorrelation analysis is performed on each pixel's transient. The value of $G_2(dt)$ is used as the intensity for each pixel in the super-resolution SOFI image and the curve fit (dashed line) obtains the diffusion coefficient, D_{calc}, which is accurate with respect to the true value, D_{sim}. (**f-l**) Results and comparison of fcsSOFI analysis. (**f**) The ground truth pore map used in the simulation. Emitters undergo 1D Brownian diffusion within the pores, with a different D_{sim} for each pore. (**g**) The diffraction-limited average image. (**h**) Centroid locations and trajectories localized by SPT analysis; different colors indicate individual trajectories. (**i**) The SOFI image produced from $G_2(dt)$ and deconvolution. (**j**) Comparison of extracted resolutions for each method, obtained from line sections averaged across all y (color corresponds to border colors in g-i). (**k**) The diffraction-limited map of D_{calc}. (**l**) The final fcsSOFI image produced by image fusion where (**i**) represents the saturation and (**k**) the hue. Scale bars = 300 nm.

transients from one pixel in each pore are show in Figure 1b, c and their respective autocorrelations are shown in Figure 1d, e. The two true pore locations (Figure 1f) are not observed in the diffraction-limited average image (Figure 1g) and are difficult to resolve by traditional SPT,[33] in which sub-diffraction-limited localization of individual PSFs is performed (Figure 1h, see Figure S6 for alternative blurred centroid representation of SPT data). As often occurs in localization microscopy, SPT mischaracterized some of the emitters to be in between the two pores (Figure S3) and incorrect tracking of emitters diffusing between the two pores occurred. In contrast, the SOFI analysis in Figure 1i revealed the presence of two pores. Figure 1j quantitatively compares the spatial resolutions obtained in each type of image. SOFI analysis resolved the pores to 158 nm, as defined by the FWHM, compared to both the diffraction-limited average image and SPT analysis, where there is no distinction between the pores at the FWHM (Figure 1j). Further, the diffraction-limited average image and SPT analysis misalign the

center locations of the pores compared to the true location due to the overlap of the PSFs (Figure S3). Advanced SPT algorithms could better localize the centroids by rejecting overlapping PSFs due to non-ideal Gaussian shapes,[34] but more subjective user input would be required[35] than the algorithm used here.[33] Comparison of data from a single pore quantified the resolution enhancement of the SOFI analysis to be up to a factor of two as compared to the diffraction-limited image (Figures S2 and S4). Similar improvements were found for simulated diffusion under flow and anomalous Lévy diffusion (Figure S5).

SOFI analysis produced super-resolution images under high throughput conditions and low SBR, unlike localization-based techniques. The quantitative comparison of diffraction-limited imaging, SPT, and SOFI analysis shown in Figure 1j was extended to SBRs ranging from 1-10 (Figure S7 and Movies S1, S2). The resolution improvement for SOFI was maintained over the broad range of SBR conditions, whereas SPT failed at lower SBRs. Additionally, correlation based super-resolution can be considered an *a priori* analysis method, whereas the filtering, multiframe association, and machine learning methods needed to broaden the utility of SPT[34] require subjective user input.[35] Therefore, for challenging single molecule experiments where adequate signal is difficult to obtain, such as those with fast diffusion or biological environments, correlation analysis has advantages over SPT.

Simulations also showed that the distribution of heterogeneous diffusion coefficients within pores is accurately obtained and mapped at sub-

diffraction levels. Curve fitting with a model for Brownian diffusion was applied to the autocorrelation decay at each individual pixel (Figure 1d, e). Calculated diffusion coefficients (D_{calc}) of D_{left} = 1.0 (± 0.1) x 10^5 nm^2/s and D_{right} =1.1 (± 0.1) x 10^4 nm^2/s were accurately extracted (≤ 10% error) and mapped in Figure 1k. Due to the high sensitivity of correlation analysis to weak fluctuations, the analysis accurately quantifies diffusion of the PSF across >2σ, producing a diffraction-limited map of diffusion characteristics. In contrast, quantitative analysis of the SPT data[33] miscalculates a stationary population of emitters with $\log(D_1/nm^2 \cdot s^{-1})$ = -8.9 (± 1.7) in addition to a diffusing population, $\log(D_2/nm^2 \cdot s^{-1})$ = 4.7 (± 1.5), due to the close proximity of the pores and density of emitters

(Figure S8). Performing image fusion between Figures 1i and 1k resulted in the final fcsSOFI image (Figure 1l) that accurately quantifies the diffusion constant within 10% at a spatial resolution of one half the diffraction limit. Further demonstration of the accuracy of fcsSOFI using 2D simulations is provided in Supporting Information (Figures S9 and S10 and Movie S3).

Experimental application of fcsSOFI to agarose and liquid crystals

fcsSOFI analysis was applied to image heterogeneous pore distribution and diffusion within agarose hydrogels, which are used broadly in cell culture growth, electrophoretic and

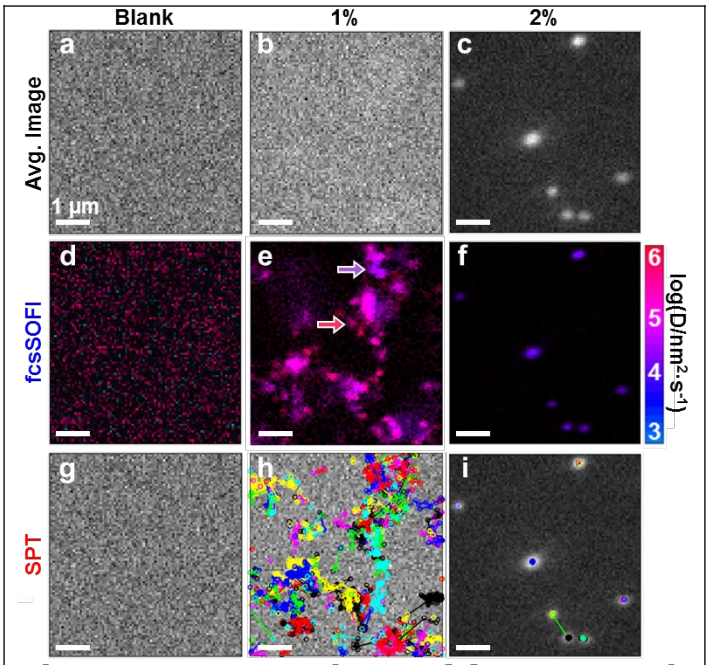

Figure 2. Comparison of fcsSOFI and SPT analyses of pore size and diffusion in an agarose gel structure. Results for 100 nm bead diffusion in (**a, d, g**) water over a blank coverslip, (**b, e, h**) 1% agarose, and (**d, f, i**) 2% agarose. (**a-c**) Diffraction-limited average images show no features in (**a**) (blank coverslip), but also incorrectly no features (contrast < 2) in (**b**) (1% agarose) due to the low excitation power used and fast diffusion. (**c**) Diffraction-limited locations of beads in 2% agarose are observed. (**d-f**) fcsSOFI maps show (**d**) unresolvable fast diffusion over the coverslip, (**e**) heterogeneous diffusion (highlighted by arrows; purple, $\log(D\ /\mathrm{nm^2 \cdot s^{-1}}) \sim 4$; red, $\log(D/\mathrm{nm^2 \cdot s^{-1}}) \sim 6$) of average $\log(D/\mathrm{nm^2 \cdot s^{-1}}) = 4.8 \pm 0.8$ in 1% agarose, and stationary $\log(D/\mathrm{nm^2 \cdot s^{-1}}) = 3.3 \pm 0.3$ in 2% agarose. Comparatively, (**g-i**) interpretation of SPT in 1 and 2% agarose is difficult due to short and overlapping trajectories. Quantitative comparisons of diffusion coefficients and pore size in (**e, f**) and (**h, i**) are in Figure S11. Scale bars are all 1 µm. Example curve fitting results of fcsSOFI analysis are shown in Figure S13. Movies of the respective data analyzed are shown in Movies S4-S6.

chromatographic separations,[9, 36] and 3D immunoassays[37] (Figure 2). Imaging the nanoscale pore structure of agarose by traditional methods is challenging due to the high water content, which undoubtedly leads to the disparity in pore sizes reported in the literature.[36, 38-40] We therefore compared fcsSOFI analysis to diffraction-limited imaging and to SPT analysis of diffusing 100 nm carboxylate fluorescent spheres in agarose. Wide-field Total Internal Reflection Fluorescence (TIRF) microscopy was used for imaging (see Methods), and a blank coverslip with the spheres in water was used as a control. Indeed, the heterogeneity in spatial and diffusion features of

the agarose could be discerned by the fcsSOFI approach (Figure 2). In comparison to the control sample in which diffusion occurred with no preferred spatial distribution, in 1% and 2% agarose the probes stochastically diffused in the pores (Movies S4-S6). The 1% average image did not resolve any structures due to fast diffusion and low SBR, whereas the 2% average image shows the diffraction-limited position of emitters that are primarily trapped within pores (Figure 2a-c). In contrast, fcsSOFI analysis revealed the heterogeneous distribution of bright areas where beads are free to diffuse (*i.e.* pores) and dark areas devoid of diffusing beads (high density agarose), and successfully mapped the pore structure for both fast-moving and slow-moving/stationary probes (Figure 2d-f).

Quantitative characterization of the spatial and diffusion properties in the 1% agarose environment showed that the fcsSOFI approach does a better job, as compared to diffraction-limited imaging and SPT, in discerning pore sizes and heterogeneous diffusion properties (Figure 2b, e, h). First, the fcsSOFI image in Figure 2e resolved pores at a 150-fold higher contrast compared to the diffraction-limited image in Figure 2b (SBR ~ 300 and ~2 for the fcsSOFI and average images, respectively). This result demonstrates the high sensitivity of correlation analysis to low signal fluctuations. Next, the fcsSOFI analysis in Figure 2e was used to determine that there are primarily two pore populations with diameters of 240 ± 90 nm and 1000 ± 500 nm (Figure S11a). SPT analysis identified only short trajectories due to the low signal and high density of emitters (mean trajectory length = 4

points; Figure 2h, Figure S11c), and yielded a smaller average pore size of 150 ± 130 nm (Figure S11a). Interestingly, if ensemble methods were used, instead of identifying the underlying heterogeneous pore distribution, a normal distribution with diameter 240 ± 90 nm, would be extracted,[39] agreeing well with one previous report.[40] Finally, for the diffusion properties, correlation analysis finds an average of $\log(D/\mathrm{nm}^2\cdot\mathrm{s}^{-1}) = 4.8 \pm 0.8$, in agreement with expectations based on FCS (Figure S11b).[41] SPT also accurately finds $\log(D/\mathrm{nm}^2\cdot\mathrm{s}^{-1}) = 5.3 \pm 0.3$. However, fcsSOFI analysis super-resolves the spatial heterogeneity of diffusion coefficients (arrows, Figure 2e). Smaller diffusion coefficients seem to arise from increased confinement within the agarose, where diffusion becomes anomalous (Figure S10). Another possibility, albeit unlikely in this case, is that there are motions in the axial direction that is not incorporated in the correlation curve fitting decay model. In contrast, it is difficult to visualize the relationship between the heterogeneous diffusion coefficients and the porous structure with a map of overlapping, short trajectories in the SPT figures. Further quantitative discussion of the experiments with 2% agarose is included in the Supporting Information where fcsSOFI analysis may not be the preferred method for analysis of stationary emitters that are trivial to track.

fcsSOFI analysis was also demonstrated to achieve super-resolved structural details from 1D diffusion of perylene diimide (DTPDI) single molecule fluorophores within lyotropic liquid crystal gels (Figure 3). Liquid crystals can controllably self-assemble into complex phase-segregated structures for applications in biological and electronic transport and electro-optical displays.[42-45] While SPT has been applied to diffusion in 1D aligned liquid crystals[11, 42] and polydimethylsiloxane nanochannels,[46] optimizing appropriate experimental conditions is a challenge. In contrast to fluorescent beads, single molecule emitters present an additional challenge due to photobleaching, which reduces the total signal observed during the measurement. Rapid diffusion also causes difficulty in linking frame-to-frame positions to form trajectories. SPT fails in cases like the data exhibited in

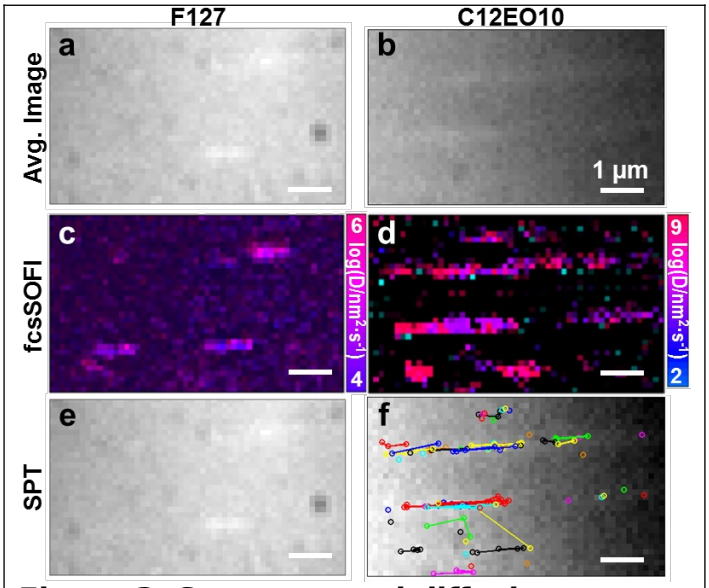

Figure 3. Structure and diffusion characterization of aqueous lyotropic liquid crystal gels by fcsSOFI compared to diffraction-limited imaging and SPT. Results for (**a, c, e**) DTPDI diffusion in F127 and (**b, d, f**) DTPDI diffusion in C12EO10. (**a, b**) The average diffraction-limited images show no noticeable features while (**c, d**) correlation reveal paths of 1D pores aligned across the structure. (**e, f**) Particle tracking cannot obtain (**e**) any particle locations in F127, while in C12EO10, particles are localized, but diffusion across paths is incorrectly identified and diffusion coefficients cannot be extracted due to the shortness of the trajectories (only two trajectories are longer than four points). Scale bars are all 1 µm. Videos of the respective data analyzed are shown in Movies S7-S8.

Moves S7 and S8 due to photobleaching and fast diffusion. Despite the limited amount of signal, fcsSOFI analysis reveals the 1D spatial alignment of pores in F127 and C12EO10 liquid crystals (Figure 3c, d). Due to fast diffusion and low SBR, the diffraction-limited average images entirely miss this 1D spatial alignment (Figure 3a, b). For F127, analysis of the diffusion coefficients were very similar to previous reports ($\log(D/\mathrm{nm}^2\cdot\mathrm{s}^{-1}) = 4.7 \pm 0.3$),[42] whereas SPT failed to localize molecules due to the low SBR (Figure 3e). For C12EO10, the low SBR posed challenges in curve fitting (Figure S12d). However, estimation of diffusion coefficients by SPT in C12EO10 was not possible due to short trajectories (Figure 3f). Further work with higher SBR and extended dye lifetimes could improve confidence in the results of fluorophore diffusion in lyotropic liquid crystals.

CONCLUSION

We introduced fcsSOFI, a new correlation-based super-resolution imaging technique to characterize the structure of and diffusion dynamics within porous nanomaterials. We showed by simulations and by experiments that fluorescence fluctuations from diffusing probes within porous spaces can be analyzed to yield information about pore sizes and diffusion coefficients. Our method does not require extensive development of experimental protocol to directly label the material compared to other super-resolution techniques; radiant probes only must be able explore the porous space. Overall, we envision that fcsSOFI could be applied to a diverse class of

porous materials, including synthetic soft polymers such as hydrogels,[1] phase separated block copolymers,[11] and polymers,[6, 10] biological environments such as the cellular cytosol[3] and membrane,[4, 5] and heterogeneous hard porous materials such as surfactant-filled mesoporous silica,[11, 47] zeolites,[2] metal-organic-frameworks,[7] and activated carbon.[8] In the latter inorganic systems with dense pore networks, the rate of diffusion and spatial alignment of pores would be expected to be able to be resolved by fcsSOFI, but a possible limitation would be resolving every single pore due to the current resolution enhancement of a factor of $\sim < 2$. It would also be interesting to combine fcsSOFI with scanning methods such as raster image correlation spectroscopy (RICS)[24, 48] and spatio-temporal image correlation spectroscopy (STICS)[49] which could produce super-resolution images with a confocal microscope geometry and on different time scales relevant to cellular processes. Future work will pursue a better understanding of the relation between the experimental parameters, analysis, and final resulting correlation images,[50] including quantifying the statistical requirements for correlation analysis,[51] the relationship between probe/pore sizes, concentrations and chemistries, quantifying more diverse types of diffusion, and obtaining spatial information in 3D.[29, 30]

METHODS

Diffusion simulation. All simulations and analysis were written in Matlab 2011b. For the simulation, we define our pixel size to be 50 nm and frame

rate to be 25 Hz to be similar to experimental conditions. Each emitter is represented by a two-dimensional Gaussian point spread function with a full width half maximum of 317 nm, approximately the diffraction limit for a 637 nm excitation wavelength. The intensity of the emitter is taken from a Poisson distribution of intensities to simulate shot noise. The background of the image is taken from a random normal distribution to simulate readout noise. For simulations of 1D diffusion, the emitters are allowed to traverse in pores separated at a sub-diffraction limit (Figure 2a, f) by 300 nm. Continuous boundaries were used at the edges. For 2D diffusion, pore maps with features separated by variable number of pixels were provided as shown in Figures S9a and S10a. Random 1D and 2D walks were used to simulate diffusion. For each step, the magnitude of the displacement is based on a user-defined diffusion coefficient and distribution width, the step size was sampled from a normal distribution and added to the particles previous location.[52] Three types of diffusion were simulated to demonstrate the versatility of the technique: Brownian (random walk), Brownian under flow (biased random walk), and anomalous diffusion (Lévy walk, step size taken from a power distribution). The number of emitters, diffusion constant, and SBR were also varied. A total of 5000 frames were analyzed in each simulation. See Movies S1-S3 for example simulations.

Experimental agarose data. Carboxylate modified polystyrene beads of 100 nm size (orange fluorescent, max abs/em: 540/560 nm, Invitrogen) were

diluted by a factor of 1:500 concentration in 1 and 2% (w/w) agarose (type I low EEO, Sigma Aldrich) in molecular biology grade water (Hyclone, VWR) heated to 80 °C. The anionic carboxyl group on the emitter beads would be expected to have minimal interaction with the anionic agarose.[41] Further discussion on the selection of possible emitters, including mixtures, for fcsSOFI is provided in the Supporting Information. Glass coverslips (No. 1, 22 x 22 mm, VWR) were cleaned for 90 s in a bath of 4% (v/v) H_2O_2 (Fisher Scientific, Radnor, PA) and 13% (v/v) NH_4OH heated to 80 °C. The slides were further cleaned under O_2 plasma (PDC-32G; Harrick Plasma; medium power) for 2 min. A custom sized silicon template (43018M, Grace BioLabs) was place on the coverslip and a 30 µL aliquot of the bead/agarose solution was added. The chamber was covered with an additional coverslip to avoid dehydration and the agarose gelled at room temperature.

An in-house constructed wide-field TIRF microscope was used to measure samples after equilibration on the microscope stage for fifteen minutes. The beam of a solid state 532 nm laser (Coherent, Compass 315M-100SL) was focused at the edge of a 1.45 NA, 100x, oil-immersion objective (Carl-Zeiss, alpha Plan-Fluar) for through-the-objective TIRF microscopy. Further details of the microscope setup have been previously reported.[53] The generated evanescent wave at the coverslip/agarose interface had an approximate intensity of 10 µW/cm^2. The low intensity was used to limit the observation volume in the axial dimensional (~ 85 nm) to avoid 3D effects on the projected 2D observation. Data were recorded with an electron-

multiplied charge coupled device (Andor, iXon 897) for 1000 frame intervals with an acquisition time of 10 ms and frame rate of 25 Hz.

Experimental 1D C12EO10 and F127 samples. The triblock copolymer Pluronic F127 having the formula $PEO_{100}PPO_{65}PEO_{100}$ was obtained from Anatrace, while decaethylene glycol monododecyl ether (C12EO10) was obtained from Sigma-Aldrich. Both were used as received. Aqueous gels of F127 and C12EO10 were prepared by first adding an appropriate amount of either to a clean, disposable glass vial. An aliquot of HPLC-grade water was then added, followed by an aliquot of n-butanol in the case of F127. The final dye-doped F127 gel composition was 47.5% F127, 38.6% water, 9.9% butanol and 4.0% ethanol (see below) by weight. The final dye-doped C12EO10 gel composition was 53.7% C12EO10, 44.1% water and 2.2% ethanol (see below) by weight. These gels were extremely viscous. They were mixed by repeated inversion and centrifugation. Air bubbles formed in the gels during mixing were removed by repeated centrifugation for several hours over a period of several days prior to use.

N,N’-bis(tridecyl)-perylene-3,4,9,10-tetracarboxylic diimide (DTPDI) was employed as the probe dye in both samples. The dye was obtained from Sigma-Aldrich and was used as received. A 96 nM solution of the dye in ethanol (HPLC grade) was used to prepare dye doped samples. The final dye concentration was ~ 5 nM and ~ 3 nM in the F127 and C12EO10 gels, respectively.

Fluidic channels were used for encapsulation and flow alignment of the F127 and C12EO10 samples, as described previously.[42] These were prepared by casting uncured poly(dimethylsiloxane) (PDMS, Sylgaard 184) onto a prefabricated glass mold. A rectangular fluidic channel of 0.5 mm depth, 2.5 mm width, and 15 mm length was obtained after curing of the PDMS and separation from the mold. Inlet and outlet holes 1.5 mm in diameter were subsequently punched in the ends of the channel. The PDMS monolith was next cleaned in an air plasma (5 min) along with a microscope cover slip (FisherFinest Premium). The PDMS monolith was then contacted to the cover slip to form the completed fluidic cell. All Movie data were collected by imaging through the cover slip.

Gels were loaded into the fluidic channels by first drawing them into a glass capillary. The capillary was next contacted to the cell inlet and the gel infused into the channel. The viscous gels were flowed into the channels at a linear flow velocity of ~ 0.5 mm/s. The small dimensions of the channel and the high viscosities of the gels ensure that channel loading occurred within the laminar flow regime. Optically clear gels were obtained in all cases. After filling, the inlet and outlet holes were sealed using standard, two-part 5 min epoxy. All samples were characterized within a few hours of preparation. The ambient temperature during sample characterization ranged from 20-22 °C. Verification that the gels comprised flow-aligned cylindrical micelles was obtained by comparing gel composition to their published phase diagrams,[54, 55] by small-angle X-ray scattering in the case of

F127 and by observation of 1D dye diffusion along the flow alignment direction in the microscope.

All DTPDI tracking experiments were performed on a wide-field fluorescence microscope operated in pseudo-TIRF mode. This system has been described previously in detail.[56] It employs an inverted epi-illumination microscope (Nikon TiE) with closed-loop focus stabilization. Light from a blue diode laser (488 nm) was used to excite dye fluorescence. The excitation light was first passed through a spinning optical diffuser before being reflected from a dichroic beamsplitter (Chroma, 505 DCLP) and focused, off-axis, into the back aperture of an oil immersion objective (Nikon Apo TIRF 100X, 1.49 numerical aperture, NA). The incident laser power was maintained at < 4 mW (< 10^3 W/cm^2) in all experiments. Fluorescence collected from the sample was passed back through the dichroic beamsplitter, through a bandpass filter (Chroma HQ535/50m) and directed onto an electron multiplying CCD (EM-CCD) camera (Andor iXon DU-897) for 400-500 frame intervals.

fcsSOFI analysis. To analyze the data, the experimental data collected by the electron-multiplied charge coupled device was converted to a MATLAB compatible format as a series of 2D images. Second order correlation was performed at each pixel over time using the built in MATLAB function 'xcorr'.[15] To avoid noise artifacts in our analysis, the resulting autocorrelation data was log binned.

To produce the super resolution image with the “new” point spread function with a resolution improvement of we use the value of $G_2(k,\tau)$ at a time lag of one frame.[15] Based on the imaging extensions of FCS,[24, 25, 57] the spatial distribution of diffusion coefficients can be obtained from curve fits of the correlation curves. From the calculated$G_2(k,\tau)$, curve fitting over all time lags is performed according to:

$$(7) G_2(k,\tau) = A(k)\frac{1}{1+\tau/\tau_D} + c$$

where *A(k)* represents the amplitude $G_2(k,0)$, *c* is a constant offset, and τ_D is the characteristic diffusion time across the pixel for which the autocorrelation was performed. This can be related to the diffusion coefficient, *D*, of the emitter by:

$$(8) D = \frac{\omega^2}{4\tau_D}$$

assuming two-dimensional Browinan diffusion, where ω the size of the detection region, a combination of the pixel size and microscope point spread function.[58] The resulting diffusion coefficient calculated at each pixel is then spatially mapped. Equations 7 and 8 can be modified for other types of diffusion including 1D Brownian (as for the simulations in Figure 1 and experimental data in Figure 3), flow, and multi-component diffusion.[24]

A super-resolution map of diffusion information is formed by fusing the spatial and diffusion results on a hue-saturation-value (HSV) colormap. The hue (H) is the normalized log of the diffusion coefficient. Diffusion

coefficients where the R^2 from curve fitting is < 0.5 are set to zero due to low confidence in the values obtained. The saturation (S) is the normalized super-resolution spatial information. Finally, the value (V) is set to a constant value of 1. The HSV matrix is then converted to RGB to provide a final fused image containing a super-resolution map of diffusion characteristics. Because the final image contains more information that the starting two images alone, the HSV method represents an image fusion technique.[31]

Analysis by particle tracking, diameter of gyration, and Delaunay triangulation. Analysis of the collected data to obtain pore size and diffusion coefficients from single particle tracking was performed by previously reported methods.[33, 59, 60] Briefly, particle tracking included steps to increase the signal-to-noise ratio, definition of a local threshold to identify possible particles, localization of particles by radial symmetry,[61] and a nearest neighbor approach to connect trajectories.[33] Analysis of the diffusion coefficient is obtained by a maximum likelihood estimation method.[62] From the respective trajectories, the radius of gyration over the entire trajectory was calculated to measure the average radius of which the probe traversed.[52, 60] The radius was then doubled to report the diameter. From the fcsSOFI images, Delaunay triangulation to discriminate irregularly shaped features was applied, with an intensity threshold for binarization two standard deviations above the mean intensity of the image, a minimum group size of five pixels, and maximum distance between neighboring points

of three pixels.[59] The total area of the identified pores was calculated by summing the grouped pixels together. The diameter was calculated by assuming a spherical pore, where $d = 2\sqrt{(area/\pi)}$.

ASSOCIATED CONTENT

Supporting Information Available: Additional information on methods and analysis, supplementary simulations, supplementary analysis of experimental data, Figures S1-S13, and Movies S1-S8. This material is available free of charge *via* the Internet at http://pubs.acs.org.

AUTHOR INFORMATION

Corresponding Author

*Phone: 713-348-4232. E-mail: cflandes@rice.edu and sweiss@chem.ucla.edu

Author Contributions

The manuscript was written through contributions of all authors. All authors have given approval to the final version of the manuscript.

ACKNOWLEDGEMENT

C. F. Landes acknowledges the Welch Foundation (C-1787), and NSF (CHE-1151647). L. Kisley thanks the NSF (GRFP 0940902). R. Brunetti acknowledges the NSF REU at the Rice Quantum Institute (PHY 1156542). S.

Weiss acknowledges Willard Chair funds. D. A. Higgins acknowledges the DOE (DE-FG02-12ER16095).

ABBREVIATIONS

FCS, fluorescence correlation spectroscopy; SOFI, super-resolution optical fluctuation imaging; fcsSOFI, fluorescence correlation spectroscopy super-resolution optical fluctuation imaging; SPT, single particle tracking; PSF, point spread function; SBR, signal-to-background ratio; TIRF, total internal reflection fluorescence; DTPDI, N,N’-bis(tridecyl)-perylene-3,4,9,10-tetracarboxylic diimide

REFERENCES

1. Yamaguchi, N.; Zhang, L.; Chae, B.-S.; Palla, C. S.; Furst, E. M.; Kiick, K. L. Growth Factor Mediated Assembly of Cell Receptor-Responsive Hydrogels. *J. Am. Chem. Soc.* **2007**, *129*, 3040-3041.

2. Ristanović, Z.; Kerssens, M. M.; Kubarev, A. V.; Hendriks, F. C.; Dedecker, P.; Hofkens, J.; Roeffaers, M. B.; Weckhuysen, B. M. High-Resolution Single-Molecule Fluorescence Imaging of Zeolite Aggregates within Real-Life Fluid Catalytic Cracking Particles. *Angew. Chem. Int. Ed.* **2014**, *54*, 1836-1840.

3. Dhar, A.; Samiotakis, A.; Ebbinghaus, S.; Nienhaus, L.; Homouz, D.; Gruebele, M.; Cheung, M. S. Structure, Function, and Folding of Phosphoglycerate Kinase Are Strongly Perturbed by Macromolecular Crowding. *Proc. Natl. Acad. Sci. USA* **2010**, *107*, 17586-17591.

4. Langecker, M.; Arnaut, V.; Martin, T. G.; List, J.; Renner, S.; Mayer, M.; Dietz, H.; Simmel, F. C. Synthetic Lipid Membrane Channels Formed by Designed DNA Nanostructures. *Science* **2012**, *338*, 932-936.

5. Wang, Y.; DeBerg, H.; Nomura, T.; Tonks-Hoffman, M.; Rohde, P.; Martinac, B.; Selvin, P. R. Measuring the Pore-Size and Dynamics of the MscL Mechanosensitive Channel Using smFRET. *Biophys. J.* **2013**, *104*, 385a.

6. Fischbach, C.; Chen, R.; Matsumoto, T.; Schmelzle, T.; Brugge, J. S.; Polverini, P. J.; Mooney, D. J. Engineering Tumors with 3D Scaffolds. *Nat. Meth.* **2007**, *4*, 855-860.

7. Liao, Y.; Yang, S. K.; Koh, K.; Matzger, A. J.; Biteen, J. S. Heterogeneous Single-Molecule Diffusion in One-, Two-, and Three-Dimensional Microporous Coordination Polymers: Directional, Trapped, and Immobile Guests. *Nano Lett.* **2012**, *12*, 3080-3085.

8. Nishihara, H.; Kyotani, T. Templated Nanocarbons for Energy Storage. *Adv. Mater.* **2012**, *24*, 4473-4498.

9. Kisley, L.; Chen, J.; Mansur, A. P.; Shuang, B.; Kourentzi, K.; Poongavanam, M.-V.; Chen, W.-H.; Dhamane, S.; Willson, R. C.; Landes, C. F. Unified Superresolution Experiments and Stochastic Theory Provide Mechanistic Insight into Protein Ion-Exchange Adsorptive Separations. *Proc. Natl. Acad. Sci. USA* **2014**, *111*, 2075-2080.

10. Reznik, C.; Estillore, N.; Advincula, R. C.; Landes, C. F. Single Molecule Spectroscopy Reveals Heterogeneous Transport Mechanisms for Molecular Ions in a Polyelectrolyte Polymer Brush. *J. Phys. Chem. B* **2009**, *113*, 14611-14618.

11. Higgins, D. A.; Tran-Ba, K.-H.; Ito, T. Following Single Molecules to a Better Understanding of Self-Assembled One-Dimensional Nanostructures. *J. Phys. Chem. Lett.* **2013**, *4*, 3095-3103.

12. Maaloum, M.; Pernodet, N.; Tinland, B. Agarose Gel Structure Using Atomic Force Microscopy: Gel Concentration and Ionic Strength Effects. *Electrophoresis* **1998**, *19*, 1606-1610.

13. Polarz, S.; Antonietti, M. Porous Materials *via* Nanocasting Procedures: Innovative Materials and Learning About Soft-Matter Organization. *Chem. Commun.* **2002**, 2593-2604.

14. Breedveld, V.; Pine, D. Microrheology as a Tool for High-Throughput Screening. *J. Mater. Sci.* **2003**, *38*, 4461-4470.

15. Dertinger, T.; Colyer, R.; Iyer, G.; Weiss, S.; Enderlein, J. Fast, Background-Free, 3D Super-Resolution Optical Fluctuation Imaging (SOFI). *Proc. Natl. Acad. Sci. USA* **2009**, *106*, 22287-22292.

16. Rust, M. J.; Bates, M.; Zhuang, X. Sub-Diffraction-Limit Imaging by Stochastic Optical Reconstruction Microscopy (STORM). *Nat. Meth.* **2006**, *3*, 793-796.

17. Betzig, E.; Patterson, G. H.; Sougrat, R.; Lindwasser, O. W.; Olenych, S.; Bonifacino, J. S.; Davidson, M. W.; Lippincott-Schwartz, J.; Hess, H. F. Imaging

Intracellular Fluorescent Proteins at Nanometer Resolution. *Science* **2006**, *313*, 1642-1645.

18. Hell, S. W.; Wichmann, J. Breaking the Diffraction Resolution Limit by Stimulated Emission: Stimulated-Emission-Depletion Fluorescence Microscopy. *Opt. Lett.* **1994**, *19*, 780-782.

19. Dedecker, P.; Mo, G. C. H.; Dertinger, T.; Zhang, J. Widely Accessible Method for Superresolution Fluorescence Imaging of Living Systems. *Proc. Natl. Acad. Sci. USA* **2012**, *109*, 10909-10914.

20. Dertinger, T.; Pallaoro, A.; Braun, G.; Ly, S.; Laurence, T. A.; Weiss, S. Advances in Superresolution Optical Fluctuation Imaging (SOFI). *Q. Rev. Biophys.* **2013**, *46*, 210-221.

21. Ruckebusch, C.; Bernex, R.; Allegrini, F.; Sliwa, M.; Hofkens, J.; Dedecker, P. Mapping Pixel Dissimilarity in Wide-Field Super-Resolution Fluorescence Microscopy. *Anal. Chem.* **2015**, *87*, 4675-4682.

22. Elson, E. L.; Madge, D. Fluorescence Correlation Spectroscopy, I. Conceptual Basis and Theory. *Biopolymers* **1974**, *13*, 1-27.

23. Petersen, N. O.; Höddelius, P. L.; Wiseman, P. W.; Seger, O.; Magnusson, K. Quantitation of Membrane Receptor Distributions by Image Correlation Spectroscopy: Concept and Application. *Biophys. J.* **1993**, *65*, 1135.

24. Kolin, D. L.; Wiseman, P. W. Advances in Image Correlation Spectroscopy: Measuring Number Densities, Aggregation States, and Dynamics of Fluorescently Labeled Macromolecules in Cells. *Cell Biochem. Biophys.* **2007**, *49*, 141-164.

25. Cooper, J. T.; Harris, J. M. Imaging Fluorescence-Correlation Spectroscopy for Measuring Fast Surface Diffusion at Liquid/Solid Interfaces. *Anal. Chem.* **2014**, *86*, 7618-7626.

26. Toplak, T.; Pandzic, E.; Chen, L.; Vicente-Manzanares, M.; Horwitz, A. R.; Wiseman, P. W. STICCS Reveals Matrix-Dependent Adhesion Slipping and Gripping in Migrating Cells. *Biophys. J.* **2012**, *103*, 1672-1682.

27. Wazawa, T.; Ueda, M., Total Internal Reflection Fluorescence Microscopy in Single Molecule Nanobioscience In *Advances in Biochemical Engineering/Biotechnology*, Rietdorf, J., Ed. Springer Berlin/Heidelberg, 2005; Vol. 95, pp 77-107.

28. Sroubek, F.; Milanfar, P. Robust Multichannel Blind Deconvolution *via* Fast Alternating Minimization. *IEEE T. Image Process.* **2012**, *21*, 1687-1700.

29. Dertinger, T.; Xu, J.; Naini, O. F.; Vogel, R.; Weiss, S. SOFI-Based 3D Superresolution Sectioning with a Widefield Microscope. *Optical Nanoscopy* **2012**, *1*, 2.

30. Geissbuehler, S.; Sharipov, A.; Godinat, A.; Bocchio, N. L.; Sandoz, P. A.; Huss, A.; Jensen, N. A.; Jakobs, S.; Enderlein, J.; Gisou van der Goot, F.*; et al.* Live-Cell Multiplane Three-Dimensional Super-Resolution Optical Fluctuation Imaging. *Nat. Commun.* **2014**, *5*, 5830.

31. Haghighat, M. B. A.; Aghagolzadeh, A.; Seyedarabi, H. A Non-Reference Image Fusion Metric Based on Mutual Information of Image Features. *Comput. Electr. Eng.* **2011**, *37*, 744-756.

32. Fernández-Suárez, M.; Ting, A. Y. Fluorescent Probes for Super-Resolution Imaging in Living Cells. *Nat. Rev. Mol. Cell Bio.* **2008**, *9*, 929-943.

33. Shuang, B.; Chen, J.; Kisley, L.; Landes, C. F. Troika of Single Particle Tracking Programing: SNR Enhancement, Particle Identification, and Mapping. *Phys. Chem. Chem. Phys.* **2014**, *16*, 624-634.

34. Chenouard, N.; Smal, I.; De Chaumont, F.; Maška, M.; Sbalzarini, I. F.; Gong, Y.; Cardinale, J.; Carthel, C.; Coraluppi, S.; Winter, M. Objective Comparison of Particle Tracking Methods. *Nat. Meth.* **2014**, *11*, 281-289.

35. Saxton, M. J. A Particle Tracking Meet. *Nat. Meth.* **2014**, *11*, 247-248.

36. Guan, J.; Wang, B.; Granick, S. Automated Single-Molecule Imaging to Track DNA Shape. *Langmuir* **2011**, *27*, 6149-6154.

37. Jokerst, J. V.; Chou, J.; Camp, J. P.; Wong, J.; Lennart, A.; Pollard, A. A.; Floriano, P. N.; Christodoulides, N.; Simmons, G. W.; Zhou, Y.*; et al.* Location of Biomarkers and Reagents within Agarose Beads of a Programmable Bio-Nano-Chip. *Small* **2011**, *7*, 613-624.

38. Valentine, M. T.; Kaplan, P. D.; Thota, D.; Crocker, J. C.; Gisler, T.; Prud'homme, R. K.; Beck, M.; Weitz, D. A. Investigating the Microenvironments of Inhomogeneous Soft Materials with Multiple Particle Tracking. *Phys. Rev. E* **2001**, *64*, 061506.

39. Pernodet, N.; Maaloum, M.; Tinland, B. Pore Size of Agarose Gels by Atomic Force Microscopy. *Electrophoresis* **1997**, *18*, 55-58.

40. Narayanan, J.; Xiong, J.-Y.; Liu, X.-Y. Determination of Agarose Gel Pore Size: Absorbance Measurements Vis a Vis Other Techniques. *J. Phys.: Conf. Ser.* **2006**, *28*, 83-86.

41. Daniels, C. R.; Kisley, L.; Kim, H.; Chen, W.-H.; Poongavanam, M.-V.; Reznik, C.; Kourentzi, K.; Willson, R. C.; Landes, C. F. Fluorescence Correlation Spectroscopy Study of Protein Transport and Dynamic

Interactions with Clustered-Charge Peptide Adsorbents. *J. Mol. Recognit.* **2012**, *25*, 435-442.

42. Kirkeminde, A. W.; Torres, T.; Ito, T.; Higgins, D. A. Multiple Diffusion Pathways in Pluronic F127 Mesophases Revealed by Single Molecule Tracking and Fluorescence Correlation Spectroscopy. *J. Phys. Chem. B* **2011**, *115*, 12736-12743.

43. Kato, T. Self-Assembly of Phase-Segregated Liquid Crystal Structures. *Science* **2002**, *295*, 2414-2418.

44. Khatua, S.; Chang, W.-S.; Swanglap, P.; Olson, J.; Link, S. Active Modulation of Nanorod Plasmons. *Nano Lett.* **2011**, *11*, 3797-3802.

45. Lee, S.; Noda, K.; Hirata, S.; Vacha, M. Position-Dependent Three-Dimensional Diffusion in Nematic Liquid Crystal Monitored by Single-Particle Fluorescence Localization and Tracking. *J. Phys. Chem. Lett.* **2015**, *6*, 1403-1407.

46. Cheng, M.-C.; Leske, A. T.; Matsuoka, T.; Kim, B. C.; Lee, J.; Burns, M. A.; Takayama, S.; Biteen, J. S. Super-Resolution Imaging of PDMS Nanochannels by Single-Molecule Micelle-Assisted Blink Microscopy. *J. Phys. Chem. B* **2013**, *117*, 4406-4411.

47. Lebold, T.; Michaelis, J.; Bräuchle, C. The Complexity of Mesoporous Silica Nanomaterials Unravelled by Single Molecule Microscopy. *Phys. Chem. Chem. Phys.* **2011**, *13*, 5017-5033.

48. Digman, M. A.; Brown, C. M.; Sengupta, P.; Wiseman, P. W.; Horwitz, A. R.; Gratton, E. Measuring Fast Dynamics in Solutions and Cells with a Laser Scanning Microscope. *Biophys. J.* **2005**, *89*, 1317-1327.

49. Hebert, B.; Costantino, S.; Wiseman, P. W. Spatiotemporal Image Correlation Spectroscopy (STICS) Theory, Verification, and Application to Protein Velocity Mapping in Living Cho Cells. *Biophys. J.* **2005**, *88*, 3601-3614.

50. Geissbuehler, S.; Bocchio, N. L.; Dellagiacoma, C.; Berclaz, C.; Leutenegger, M.; Lasser, T. Mapping Molecular Statistics with Balanced Super-Resolution Optical Fluctuation Imaging (bSOFI). *Optical Nanoscopy* **2012**, *1*, 1-7.

51. Tcherniak, A.; Reznik, C.; Link, S.; Landes, C. F. Fluorescence Correlation Spectroscopy: Criteria for Analysis in Complex Systems. *Anal. Chem.* **2008**, *81*, 746-754.

52. Tauzin, L. J.; Shuang, B.; Kisley, L. M.; Mansur, A. P.; Chen, J.; de Leon, A.; Advincula, R. C.; Landes, C. F. Charge-Dependent Transport Switching of

Single Molecular Ions in a Weak Polyelectrolyte Multilayer. *Langmuir* **2014**, *30*, 8391-8399.

53. Kisley, L.; Chang, W.-S.; Cooper, D.; Mansur, A. P.; Landes, C. F. Extending Single Molecule Fluorescence Observation Time by Amplitude-Modulated Excitation. *Methods Appl. Fluoresc.* **2013**, *1*, 037001.

54. Holmqvist, P.; Alexandridis, P.; Lindman, B. Modification of the Microstructure in Block Copolymer-Water-"Oil" Systems by Varying the Copolymer Composition and the "Oil" Type: Small-Angle X-Ray Scattering and Deuterium-NMR Investigation. *J. Phys. Chem. B* **1998**, *102*, 1149-1158.

55. Mitchell, D. J.; Tiddy, G. J.; Waring, L.; Bostock, T.; McDonald, M. P. Phase Behaviour of Polyoxyethylene Surfactants with Water. Mesophase Structures and Partial Miscibility (Cloud Points). *J. Chem. Soc. Faraday Trans.* **1983**, *79*, 975-1000.

56. Ba, K. H. T.; Everett, T. A.; Ito, T.; Higgins, D. A. Trajectory Angle Determination in One Dimensional Single Molecule Tracking Data by Orthogonal Regression Analysis. *Phys. Chem. Chem. Phys.* **2011**, *13*, 1827-1835.

57. Liu, H.; Dong, C.; Ren, J. Tempo-Spatially Resolved Scattering Correlation Spectroscopy under Dark-Field Illumination and Its Application to Investigate Dynamic Behaviors of Gold Nanoparticles in Live Cells. *J. Am. Chem. Soc.* **2014**, *136*, 2775-2785.

58. Boening, D.; Groemer, T. W.; Klingauf, J. Applicability of an EM-CCD for Spatially Resolved TIR-ICS. *Opt. Express* **2010**, *18*, 13516-13528.

59. Chen, K.; Anthony, S. M.; Granick, S. Extending Particle Tracking Capability with Delaunay Triangulation. *Langmuir* **2014**, *30*, 4760-4766.

60. Elliott, L. C.; Barhoum, M.; Harris, J. M.; Bohn, P. W. Trajectory Analysis of Single Molecules Exhibiting Non-Brownian Motion. *Phys. Chem. Chem. Phys.* **2011**, *13*, 4326-4334.

61. Parthasarathy, R. Rapid, Accurate Particle Tracking by Calculation of Radial Symmetry Centers. *Nat. Meth.* **2012**, *9*, 724-726.

62. Shuang, B.; Byers, C. P.; Kisley, L.; Wang, L.-Y.; Zhao, J.; Morimura, H.; Link, S.; Landes, C. F. Improved Analysis for Determining Diffusion Coefficients from Short Single-Molecule Trajectories with Photoblinking. *Langmuir* **2013**, *29*, 228-234.

TABLE OF CONTENTS GRAPHIC